Numerical Simulations of Two-Layer Flow past Topography. Part I: The Leeside Hydraulic Jump

RICHARD ROTUNNO AND GEORGE H. BRYAN

National Center for Atmospheric Research, Boulder, Colorado

ABSTRACT

Laboratory observations of the leeside hydraulic jump indicate it consists of a statistically stationary turbulent motion in an overturning wave. From the point of view of the shallow-water equations (SWE), the hydraulic jump is a discontinuity in fluid-layer depth and velocity at which kinetic energy is dissipated. To provide a deeper understanding of the leeside hydraulic jump, three-dimensional numerical solutions of the Navier–Stokes equations (NSE) are carried out alongside SWE solutions for nearly identical physical initial-value problems. Starting from a constant-height layer flowing over a two-dimensional obstacle at constant speed, it is demonstrated that the SWE solutions form a leeside discontinuity owing to the collision of upstream-moving characteristic curves launched from the obstacle. Consistent with the SWE solution, the NSE solution indicates the leeside hydraulic jump begins as a steepening of the initially horizontal density interface. Subsequently, the NSE solution indicates overturning of the density interface and a transition to turbulence. Analysis of the initial-value problem in these solutions shows that the tendency to form either the leeside height–velocity discontinuity in the SWE or the overturning density interface in the exact NSE is a feature of the inviscid, nonturbulent fluid dynamics. Dissipative turbulent processes associated with the leeside hydraulic jump are a consequence of the inviscid fluid dynamics that initiate and maintain the locally unstable conditions.

1. Introduction

In a laboratory study of single- and two-layer fluid flow past a submerged obstacle, Long (1954) showed that, under certain conditions, a hydraulic jump occurs on the lee side. Figure 8 of Long (1954) indicates the leeside hydraulic jump takes the form of the turbulent "reverse roller" (Fig. 1), well known to hydraulic engineers (Tschantz and Wright 2011). From a theoretical point of view, the shallow-water equations (SWE) provide a tractable mathematical description of the single- and two-layer fluid flow past an obstacle (Long 1954; Houghton and Kasahara 1968). The hydraulic jump is represented in the SWE as a discontinuity in fluid-layer depth and velocity at which kinetic energy is dissipated (e.g., Baines 1995, section 2.3.1). As noted by the latter (Baines 1995, p. 37), "The mechanisms for this energy dissipation depend on the detailed internal dynamics of the jump." The internal dynamics of the leeside jump was the focus of Rotunno and Smolarkiewicz (1995), who used physical reasoning and a two-dimensional

nonhydrostatic model to deduce the mechanism of reverse-roller–hydraulic-jump formation (see their Fig. 3). However, the two dimensionality of their model precluded the development of the three-dimensional turbulence associated with the reverse roller. In the present article, we analyze three-dimensional numerical simulations that capture the formation of the reverse roller and the subsequent transition to turbulence.

A motivating question for this research is the extent to which the detailed internal dynamics of the hydraulic jump contributes to the understanding of the downstream flow. For a classic hydraulic jump in a single-layer fluid (Rayleigh 1914), energy is dissipated in that layer; however, in a two-layer fluid, energy may be dissipated in the upper or lower fluid (Baines 1995, section 3.5). Klemp et al. (1997, section 5) argued that in a Boussinesq, two-layer system, a jump propagating into a quiescent fluid has most of its dissipation downstream of the jump at the interface between the lower and upper fluids (e.g., Wood and Simpson 1984, their Fig. 1a); in this case, the upper-layer velocity is locally reduced, and the lower-layer velocity is locally increased (Klemp et al. 1997, their Figs. 4 and 15). If, on the other hand, there is

---

Corresponding author: Richard Rotunno, rotunno@ucar.edu

FIG. 1. Schematic diagram of the flow in a ''reverse roller.''

considerable ambient shear of the opposite sense to that produced baroclinically by the inclined interface of the jump, that interface will roll upstream into the ambient flow (Wood and Simpson 1984, their Fig. 9) creating local convective instability, leading to dissipation in the lower layer, much like a breaking wave in a non-Boussinesq single-layer fluid (Klemp et al. 1997, their Figs. 5 and 16). Klemp et al. (1997, section 6) hypothesized that the Boussinesq leeside hydraulic jump is of the latter type (dissipation in the lower layer); the present Navier–Stokes equations (NSE) simulations support this hypothesis.

The physical setup for the present NSE solutions is designed to closely parallel the physical content of the two-layer SWE; the main difference is that a continuous transition (instead of a discontinuity) in potential temperature separates the lower and upper layers in the NSE initial condition. Although both the present SWE and NSE treat flow over a two-dimensional ridge, the computational domain for the NSE is three-dimensional, as required for the simulation of turbulent motion. Moreover, the NSE are solved for a Reynolds number of approximately 5000, which, although low for the real atmosphere, is high enough for the production of turbulent motion. Hence, the present simulations are in the category of direct numerical simulations (DNS) of turbulence. It will be shown that these simulations give a credible version of the mean and turbulent internal dynamics of the atmospheric (i.e., Boussinesq) hydraulic jump.

In a related study, Epifanio and Qian (2008, hereafter EQ08) performed a large-eddy simulation (LES) of a breaking two-dimensional mountain wave in an infinitely deep atmosphere characterized by constant wind U and static stability N^2. EQ08 showed that the wake due to the breaking mountain wave is due to eddies modifying the structure of the mountain wave and that energy dissipation is essential for allowing this modified mountain-wave structure to persist downstream. Despite the very different vertical distribution of $N^2(z)$ used here (in analogy with the two-layer SWE), the present results concerning the structure of the leeside wave-breaking region are qualitatively similar to those found in EQ08. As the present NSE calculations are specifically designed to explore the internal dynamics of the Boussinesq, two-layer, SWE leeside hydraulic jump, the similarity of the present results to those of EQ08 support the identification of leeside wave

breaking in a continuously stratified flow with the leeside hydraulic jump in a two-layer fluid.

Another, related motivation for the present study is that SWE simulations of vortices in the lee of three-dimensional obstacles are indifferent to the motion internal to the hydraulic jump and depend only on its energy-dissipation property (Schär and Smith 1993, their Fig. 2), whereas NSE simulations suggest a definite connection between the obstacle-scale fluid motion and the lee vortices (Rotunno et al. 1999, their Fig. 2). In R. Rotunno and G. H. Bryan (2018, unpublished manuscript, hereafter Part II), we present NSE simulations of the same two-layer flow past a three-dimensional obstacle. The analysis of these simulations provides a framework for reconciling differing interpretations of lee-vortex formation.

In section 2, we use the two-layer SWE to examine the initial evolution of the flow past an obstacle immersed in the lower layer. In section 3, we describe the physical setup of the NSE, which closely parallels that of the SWE solutions in section 2. Also described in section 3 is the numerical setup that allows for three-dimensional turbulent motion in the context of flow over a two-dimensional obstacle. Our analysis of the NSE solution is given in section 3c, which occupies the bulk of this paper. The conclusions are summarized in section 4.

2. Two-layer flow past a submerged obstacle in the SWE

a. Numerical integration of an initial-value problem

The two-layer, one-dimensional SWE in the limit where the lower layer is much thinner than the total depth of the two-fluid system may be written as

$$\partial_t u + u\partial_x u + g'\partial_x h + g'\partial_x H = 0, \qquad (1)$$

$$\partial_t h + \partial_x(uh) = 0 \qquad (2)$$

(Baines 1995, p. 95 and section 3.1), where $u(x, t)$ and $h(x, t)$ are, respectively, the lower-layer velocity and depth and $H(x)$ gives the shape of the obstacle; the along-flow coordinate is denoted by x and time by t. The reduced gravity $g' = (1 - \rho_U/\rho_L)g$, where g is the acceleration due to gravity and ρ_U and ρ_L denote the densities of the upper and lower fluids, respectively. For this study, the obstacle is specified by

$$H(x) = \begin{cases} H_m \cos^2\left(\dfrac{\pi}{2}\dfrac{|x - x_c|}{a}\right) & \text{for} \quad \dfrac{|x - x_c|}{a} \le 1 \\ 0 & \text{otherwise} \end{cases}, \quad (3)$$

where H_m is the maximum height, x_c is the center, and a is the half width of the obstacle. We consider the initial-value
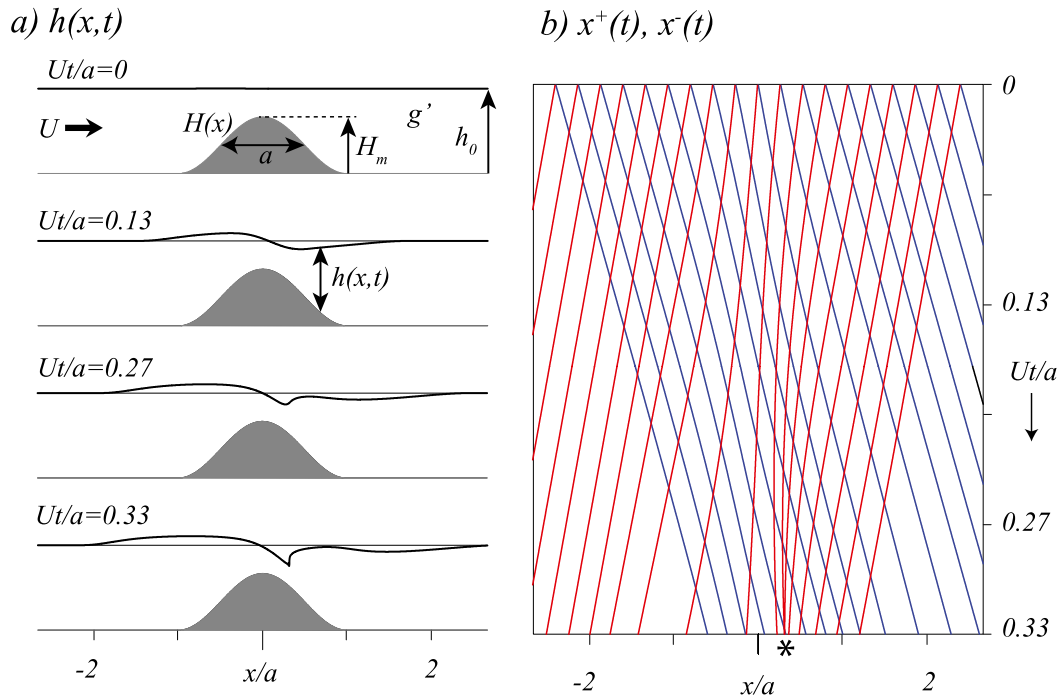
a) h(x,t)

b) $x^+(t), x^-(t)$

FIG. 2. (a) Time sequence of layer thickness $h(x, t)$ from the solution of the SWE. Input parameters are the initial layer depth h_0, obstacle height H_m, half-width a, flow speed U, and reduced gravity g'. The solution is for $U/\sqrt{g'h} = 0.22$ and $H_m/h_0 = 0.67$, where, according to Houghton and Kasahara (1968, their Fig. 3), a stationary hydraulic jump is expected on the lee side of the obstacle. (b) Characteristics curves $x^+(t)$ (blue) and $x^-(t)$ (red) for the solution shown in (a). The asterisk marks the collision point of the x^- characteristics, signifying the formation of a discontinuity.

problem, $u(x, 0) = U$ and $h(x, 0) = h_0 - H(x)$, where h_0 is the initial height of the layer (Fig. 2a).

For the numerical solution of (1) and (2), the x derivatives are discretized using centered differences on a staggered grid. The time derivatives are also approximated by a centered difference, and the leapfrog method is used to advance the solution. For the present calculation, we take $U = 5\,\mathrm{m\,s}^{-1}$, $h_0 = 1500\,\mathrm{m}$, $H_m = 1000\,\mathrm{m}$, $a = 1500\,\mathrm{m}$, and $g' = 0.34\,\mathrm{m\,s}^{-2}$. The computational domain is $-4 \le x \le 4\,\mathrm{km}$ with a grid interval $\Delta x = 4\,\mathrm{m}$. Although open boundary conditions are used, no signal reaches the domain boundaries over the time of integration. According to theory, the nondimensional numbers $U/\sqrt{g'h_0} = 0.22$ and $H_m/h_0 = 0.67$ indicate a stationary leeside hydraulic jump at steady state (Houghton and Kasahara 1968, their Fig. 3). Figure 2a shows $h(x, t)$ at various times as the flow evolves toward the discontinuity predicted by the steady-state theory. The integration is carried out (with a time step $\Delta t = 0.05\,\mathrm{s}$) until a discontinuity forms at $t \approx 100\,\mathrm{s}$ ($Ut/a \approx 0.33$).

b. Solution analysis by the method of characteristics

The approach to a discontinuity in the solution of (1) and (2) underlines the inviscid dynamics of hydraulic-jump formation. To gain a little more insight into the inviscid dynamics, (1) and (2) can be written in the characteristic form,

$$\frac{d}{dt}\left(u \pm 2\sqrt{g'h}\right) = -g'\partial_x H, \qquad (4)$$

on the respective characteristic curves given by

$$\frac{dx^\pm}{dt} = u \pm \sqrt{g'h} \qquad (5)$$

(Whitham 1974, p. 122). The equations in characteristic form can be integrated to yield the solution (u, h) (Whitham 1974, section 5.4); however, here we use the numerical solution of (1) and (2) to construct the characteristic curves that we believe provide a deeper understanding of the solution. Figure 2b shows the characteristic curves for the downstream- and upstream-moving characteristics [$x^+(t)$ and $x^-(t)$, respectively]. In general, the intersection points of the respective characteristic curves at time t give the unique solution (u, h) [since $u \pm 2\sqrt{g'h}$ are known on the characteristics by (4)]. Figure 2b shows, however, that at the point indicated by the asterisk, the upstream-moving characteristics

converge, indicating an overdetermined solution, implying the formation of a discontinuity. These conclusions are consistent with the analysis of the formation of moving leeside discontinuities given in Baines (1995, section 2.3).

To proceed with the integration beyond the time of discontinuity formation, (1) and (2) continue to hold on either side of the discontinuity; however, at the discontinuity, a condition must be imposed that is consistent with the principles of mass and momentum conservation. The discontinuity under these imposed conditions represents the hydraulic jump (Stoker 1957, section 10.6). As discussed in Klemp et al. (1997, section 6), in a Boussinesq, two-layer system, there is choice of jump condition to be made depending on the jump's internal dynamics, and therefore, the SWE for a Boussinesq, two-layer system cannot be considered a closed system without further information on the internal dynamics of the jump.

3. Two-layer flow past a submerged obstacle in the NSE

a. Numerical setup

To simulate the flow within the hydraulic jump, one needs to solve equations that are less restrictive than the SWE. In this section, we describe numerical solutions using Cloud Model 1 (CM1; Bryan and Fritsch 2002). CM1 is a general-purpose nonhydrostatic cloud model written in terrain-following coordinates. Although the fully compressible, non-Boussinesq equations are solved, the atmosphere is nearly incompressible and Boussinesq under the conditions of the present study. Thus, for ease of interpretation, we write the incompressible governing equations for momentum, energy, and mass, respectively, as

$$\partial_t \mathbf{u} + \mathbf{u} \cdot \nabla \mathbf{u} = -\nabla P + b\mathbf{k} + \nu \nabla^2 \mathbf{u}, \qquad (6)$$

$$\partial_t \theta + \mathbf{u} \cdot \nabla \theta = \kappa \nabla^2 \theta, \qquad (7)$$

$$\nabla \cdot \mathbf{u} = 0, \qquad (8)$$

where $\mathbf{u}$ is the velocity vector and θ is the potential temperature. The Boussinesq pressure variable $P = c_p \theta_{00} \tilde{\pi}$, where θ_{00} is a constant, $\tilde{\pi} = \pi - \pi_{00}(z)$, $\pi_{00}(z) = \pi_{00}(0) - gz/(c_p \theta_{00})$, where π is the Exner function, c_p is the heat capacity of dry air at constant pressure, g is the acceleration due to gravity, and (x, y, z) define the Cartesian coordinates used in our analysis. The buoyancy variable $b = g(\theta - \theta_{00})/\theta_{00}$, ν is the viscosity, and κ is the thermal diffusivity. We will refer to (6)–(8) as the NSE.

To emulate the physical problem represented by the two-layer SWE in the NSE, we consider the following base-state potential temperature:

$$\theta_0(z) = \begin{cases} \theta_L & \text{for} \quad 0 \le z \le h_0 - \delta \\ \theta_L + 0.5(\theta_U - \theta_L)(z - h_0 + \delta)/\delta & \text{for} \quad h_0 - \delta \le z \le h_0 + \delta, \\ \theta_U & \text{for} \quad h_0 + \delta \le z \le D \end{cases} \qquad (9)$$

where θ_L and θ_U are, respectively, the lower- and upper-layer potential temperatures. The variables h_0 and 2δ are the respective midpoint height and thickness of the transition layer, which is used given the difficulty treating discontinuities in a finite-difference model; thus, a third (transition) layer is unavoidable;[1] D is the height of the domain. Following the SWE calculation, we let $h_0 = 1500$ m; we let $\delta = 500$ m to ensure a well-resolved layer; a case with $\delta = 50$ m, although not as well resolved, will also be discussed for comparison. In the present calculations, $\theta_L = 288$ and $\theta_U = 298$ K so that the reduced gravity $g' = 2g(\theta_U - \theta_L)/(\theta_U + \theta_L) \approx 0.34$. The velocity is initialized with $\mathbf{u} = (U, 0, 0)$ (which adjusts to potential flow over the obstacle within a few tens of seconds), where $U = 5 \text{ m s}^{-1}$ and the potential temperature is initialized with $\theta = \theta_0(z)$. The obstacle is specified by (3) with $H_m = 1000$ m and $a = 1500$ m, as used for the SWE calculation in Fig. 2. With these external parameters specified, the nondimensional numbers $U/\sqrt{g'h_0} = 0.22$ and $H_m/h_0 = 0.67$, as well as the advective time scale a/U, are the same as for the SWE solution shown in Fig. 2. For the present calculation $\nu = \kappa = 1 \text{ m}^2 \text{ s}^{-1}$; using H_m as a length scale, the Reynolds number $UH_m/\nu = 5000$, which, while low compared to the real atmosphere, is large enough to allow turbulent flow.

"Open" boundary conditions are used at the upstream and downstream boundaries ($x = \pm 7.68$ km). Free-slip conditions are imposed at the impermeable vertical boundaries located at $z = H(x)$ and $z = 3.84$ km. Periodic conditions are imposed at the spanwise boundaries ($y = \pm 1.92$ km). The grid spacing is uniform with $\Delta x = \Delta y = \Delta z = 20$ m; the time step is $\Delta t = 0.1$ s, and the integrations are carried out until a statistical steady state is achieved in the vicinity of the obstacle (approximately 30 min). An additional 30 min of simulation

---

[1] We note that since the profile (9) implies that $\partial_z \theta_0$ depends on z, there will be a slow change of θ_0 produced by the diffusion term in (7), which, however, produces negligible changes to θ over the integration period.

is done to improve the analysis of the turbulence statistics. The numerical methods used to integrate the equations are the same as reported in Bryan and Rotunno (2014, p. 454).

b. Results

Figure 3 contains an overview of the evolution of the y-averaged (indicated by the angle brackets) flow and potential temperature over the full domain. As predicted by the SWE solution (Fig. 2), the NSE solution (Fig. 3b) indicates a steepening of the isentropes on the lee slope. This steepening signals the beginning of lee-side isentrope overturning, which, in turn, leads to a counterclockwise-rotating warm anomaly breaking off in the cool layer (Fig. 3c); likewise, cool air above the warm anomaly breaks off into a clockwise-rotating cool anomaly. These initial anomalies are followed by a continuing sequence of such anomalies that give rise to turbulence, which mixes out the anomalies over some distance (Fig. 3d). The flow essentially reaches a statistical steady state as a further 30 min of integration shows little change in the spanwise-averaged flow and potential temperature distribution (Fig. 3e).[2] Another feature of interest is that, as predicted in the SWE solution (Fig. 2a), the NSE solution (Figs. 3a,b) has a wave of elevation propagating upstream. Since the NSE solution is on a domain of finite depth, there is an acceleration of the fluid above, in addition to the expected deceleration of the fluid below, the transition layer; the velocity magnitude on the center isentrope stays close to its initial value ($5 \, \mathrm{m \, s^{-1}}$).

The SWE solution (Fig. 2) has a discontinuity forming at $Ut/a \approx 0.33$ while the NSE solution (Fig. 3) appears to form much more slowly. Estimating from Fig. 3, the dimensional time for the formation of a vertical isentrope as $t \approx 10$ min, the discontinuity forms at $Ut/a \approx 2.0$. This slower development is almost certainly because the thick transition layer, when tilted, produces smaller baroclinity as compared to a sharp transition. Figure 4 shows selected times in the evolution of a case with a thin transition layer ($\delta = 50$ m); the time for the formation of a vertical isentrope is about 5 min, and thus, $Ut/a \approx 1.0$; moreover, the sequence of eddies forming and breaking off occurs at an accelerated pace. As expected, because of the less-well-resolved transition layer, three-dimensional turbulent mixing is not as thorough, as evidenced by the occurrence of two-dimensional structures continuing to appear in the y averages even at advanced times. Other than these flow

---

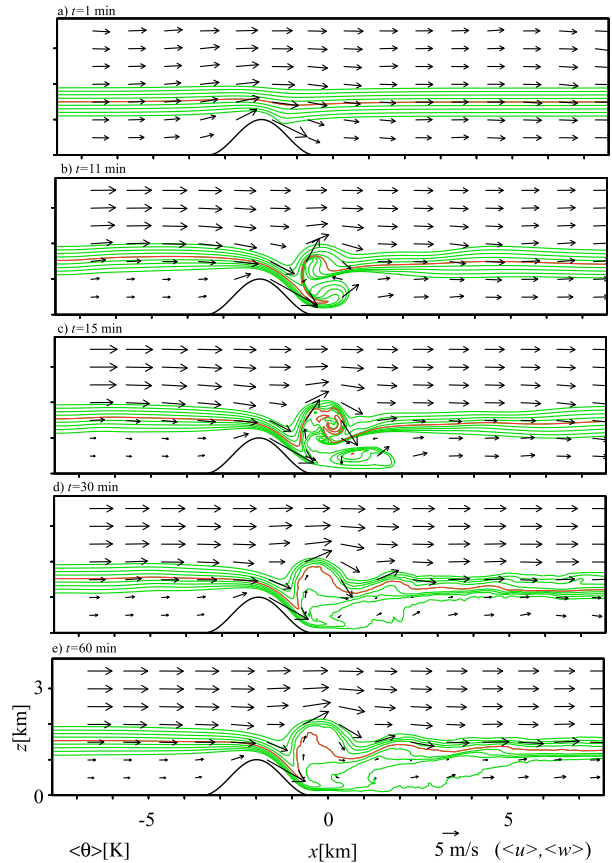[2] The total integration time of 60 min corresponds to a nondimensional time $Ut/a = 12$.

FIG. 3. Isolines of $\langle \theta \rangle$ in intervals of 1 K starting with 290 K (green contour lines, with the 294-K contour in red) and vectors representing ($\langle u \rangle$, $\langle w \rangle$) for t = (a) 1, (b) 11, (c) 15, (d) 30, and (e) 60 min. Angle brackets here and throughout indicate the y average.

details, the structure of the statistically steady flow downstream in this thin-layer simulation is qualitatively similar to that in the thick-layer simulation (cf. Figs. 3e and 4e).

One final test was motivated by the nonhydrostatic effects our steep hill might have on the solution. Two-dimensional simulations (not shown) with $a = 15\,000$ km indicated essentially the same tendencies as exhibited in the early stages of Fig. 3. This outcome is consistent with the shallow-water theory since the converging characteristic curves (Fig. 2b) imply a contracting horizontal scale, and thus a violation of the hydrostatic assumption, independent of the obstacle's horizontal scale.

Returning to the thick-layer simulation, Fig. 5 shows a more detailed view of the initial development of the y-averaged flow before the onset of turbulence (signaled by the development of turbulent kinetic energy, defined below). Figure 5a shows $\langle \theta \rangle$ and the flow vectors $\langle u \rangle$ and $\langle w \rangle$ at $t = 1$ min; isentropes are advected downward on the lee slope by the initial potential flow. In the next few
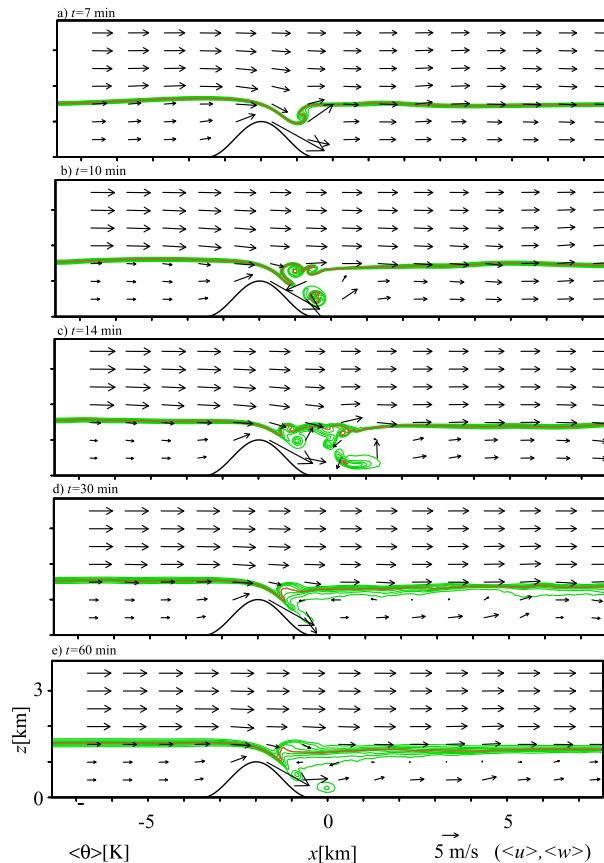
FIG. 4. As in Fig. 3, but with a thin inversion and for t = (a) 7, (b) 10, (c) 14, (d) 30, and (e) 60 min.

FIG. 5. Isolines of $\langle\theta\rangle$ and vectors as in Fig. 3 displayed on a smaller domain, with shaded regions indicating the y vorticity component $\langle\eta\rangle$ at t = (a) 1 and (b) 11 min.

minutes, there is continued steepening of the leeside isentropes, consistent with the SWE solutions in Fig. 2. At t = 11 min, Fig. 5b indicates this steepening continues to an overturning of the isentropes. Superimposed in color shading is $\langle\eta\rangle$, where η is the vorticity component in the y direction. As the flow is statistically homogeneous in y, one can infer the y-averaged flow through the inversion of $\langle\eta\rangle$ for $\langle\psi\rangle$, the streamfunction, through solution of

$$(\partial_{xx} + \partial_{zz})\langle\psi\rangle = \langle\eta\rangle, \qquad (10)$$

where $(\langle u\rangle, \langle w\rangle) = (\partial_z, -\partial_x)\langle\psi\rangle$ by virtue of (8). Qualitatively, one expects counterclockwise (clockwise) flow around centers of negative (positive) $\langle\eta\rangle$ in the perspective of Fig. 5 and subsequent figures.

Note the development of negative $\langle\eta\rangle$ in the descending flow and positive $\langle\eta\rangle$ in the reascending flow is similar to that shown in Fig. 3 of Rotunno and Smolarkiewicz (1995). The main difference is that, in the latter non-Boussinesq case, the positive vorticity is much smaller in magnitude than the negative, whereas in the
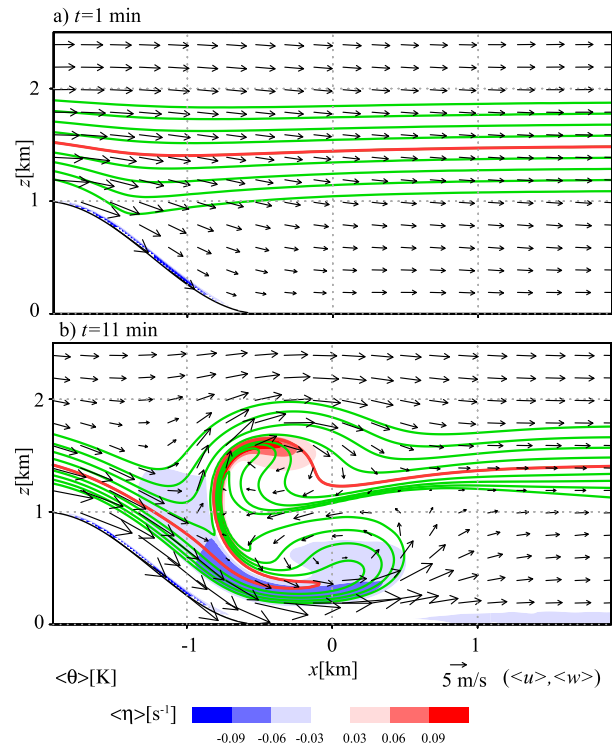
present Boussinesq example, the two have nearly equal magnitude. Hence, in the present Boussinesq case, the flow in the incipient hydraulic jump is more of a vortex dipole than a reverse-roller (negative $\langle\eta\rangle$ dominant) flow that is a hallmark of the water–air system.

The further evolution of the flow toward a statistical steady state is shown in Fig. 6. Prominent features of the flow shown in Fig. 6a are the entrainment of warmer air from the upper layer into the colder lower layer and the reverse process of colder lower-layer air being mixed with warmer upper-layer air. Negative $\langle\eta\rangle$, produced on the downward-sloping transition layer upstream, is transported into the lower layer while positive $\langle\eta\rangle$, produced on the upward-sloping part of the split transition layer, is transported into the upper layer. In this period, the flow transitions to fully three-dimensional turbulence. A statistical steady state is reached by approximately t = 30 min (Fig. 6b).

Figure 7a shows the time- and y-averaged fields (indicated by $\langle\bar{c}\rangle$, where c is a generic variable) over the period t = 30−60 min, during which the flow is approximately statistically stationary. The dipole structure in the vorticity field, evident in the initial evolution (Fig. 5), persists into the statistically steady state; the leading edge of this structure defines the NSE analog of
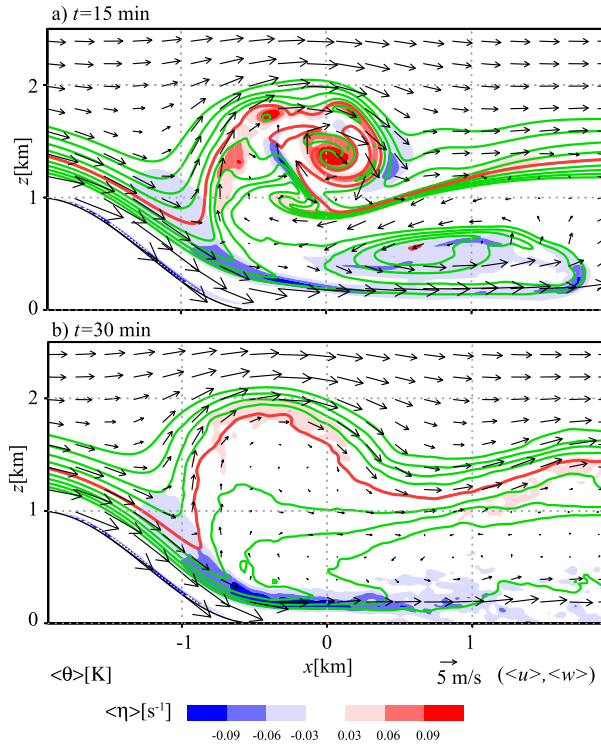
FIG. 6. As in Fig. 5, but for $t =$ (a) 15 and (b) 30 min.

FIG. 7. (a) As in Fig. 5, but for the $t = 30$–60-min average and (b) the turbulent kinetic energy averaged over the same period.

the hydraulic jump. Figure 7b shows the time- and y-averaged turbulent kinetic energy:

$$\text{tke} = \frac{\overline{\langle u'^2 + v'^2 + w'^2 \rangle}}{2}, \qquad (11)$$

where a prime indicates a deviation from the time and y average. The tke field indicates that the region enclosed by the vortex dipole is turbulent with the most intense turbulence associated with the lower shear layer. Figure 7b indicates the layer-average tke $\approx 10\,\text{m}^2\,\text{s}^{-2}$ (near $x = 1$ km), while Fig. 7a suggests $\langle u \rangle \approx 10\,\text{m}\,\text{s}^{-1}$; the ratio $\text{tke}/\langle u \rangle^2 \approx 0.1$, which is comparable to observed values (Townsend 1976, their Fig. 6.6a). Inspection of the time-dependent results (not shown) indicates instabilities growing and advecting along this lower shear layer with distance from the point where it enters the cool air (near the base of the obstacle). The instability leads to turbulence, which diffuses the vorticity (see below) and mixes the warm air into the cool layer. This split/dipole flow (Fig. 7a), as well as the distribution of tke (Fig. 7b), are similar to those found by EQ08 (their Figs. 7–9).

We have carried out two further simulations (not shown) with the grid spacing either halved or doubled; the structure of the $\langle \theta \rangle$ and tke fields is generally the same, both qualitatively and quantitatively. Moreover,
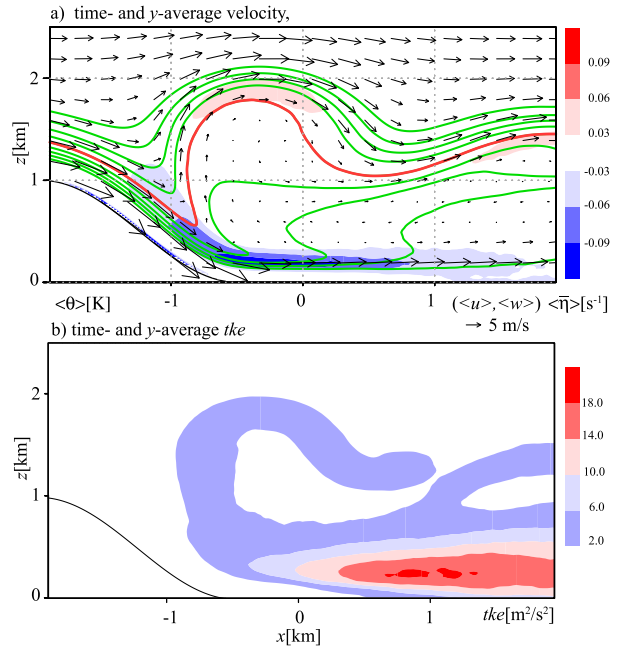
spectra computed in the spanwise (homogeneous) dimension in the turbulent regions for simulations with 10- and 20-m grid spacings have at least a decade of a $k^{-5/3}$ structure (k is the wavenumber), indicating a turbulent flow with an energy cascade.

c. Analysis

As a consequence of the two-dimensionality of the obstacle [see (3)], the initial evolution of the NSE solution is two-dimensional (Fig. 5). Moreover, as the initial-state in (9) is designed to approximate the two-layer state treated by the SWE, the dynamics of SWE, which is based on the hydrostatic (long wave) approximation, gives a qualitatively correct picture of the early flow evolution; however, as the interface between the lower and upper layers steepens and tends toward a discontinuity, the long-wave approximation locally breaks down. Although one can continue the SWE integrations by employing a "shock" condition at the location of the discontinuity formation (Stoker 1957), in the two-layer system, the choice of shock condition depends on the internal dynamics of the shock/hydraulic jump (Klemp et al. 1997, section 6), which cannot be obtained without appeal to either laboratory observations and/or numerical integrations using a less approximate set of equations as done here. In this section, we present an analysis of the leeside hydraulic jump in the NSE from its formation through to its statistical steady state.

The evolution of the y-averaged motion in the present case can be viewed through the equations for $\langle\eta\rangle$, which derives from the y component of the curl of (6):

$$\partial_t\langle\eta\rangle = -\partial_x\langle b\rangle - \nabla\cdot\langle\mathbf{J}^\eta\rangle, \qquad (12)$$

where

$$\mathbf{J}^\eta = (u\eta - \upsilon\xi - \nu\partial_x\eta, w\eta - \upsilon\zeta - \nu\partial_z\eta) \qquad (13)$$

and (ξ,ζ) are the respective (x,z) components of the vorticity vector (ξ,η,ζ). The first term on the rhs of (12) represents baroclinic generation, and the second term is the generalized transport term, with $\mathbf{J}^\eta$ representing the advective plus viscous flux of η. Equations (12) and (7) along with the inversion given in (10) together constitute the main diagnostic tool used here.

The mathematical connection between the SWE- and the NSE-based vorticity equation was reviewed in Rotunno and Smolarkiewicz (1995, section 2c). Briefly, in a two-layer nonturbulent fluid, all the terms in (12) vanish except at the interface between the upper and lower layers, at which η is produced baroclinically and advected. Figure 2 of Rotunno and Smolarkiewicz (1995) contains a schematic diagram of the vorticity distribution implied in the SWE solution for a flow like that shown in Fig. 2; note the leeside dominance of $\eta < 0$ produced where the interface $\partial_x h < 0$ (which implies $-\partial_x b < 0$).

Figure 8 shows terms in (12) with the baroclinic term in black contours and the transport term in color shading. At $t = 11$ min (Fig. 8a), the flow is not yet turbulent, and the y-averaged fields are equal to the unaveraged fields at any y location. Note first that baroclinic generation is negative on the descending isentropes over the lee slope and that this generation is exactly cancelled[3] by transport to the local negative minimum η seen in Fig. 5b. The rest of Fig. 8a describes the continuing evolution of η through baroclinic generation and advection. A notable feature of this evolution is the reversed flow induced [via (10)] by the distribution of $\eta < 0$ (Fig. 5b); this reversed flow overturns the transition layer and leads to its splitting into an upward-tilted branch, which baroclinically produces positive η, in addition to the upstream, downward-tilted branch, which produces negative η. The absence of turbulent diffusion and weak viscous dissipation at this stage indicate no

---

[3] The thin layer of transport on the obstacle corresponds to the vorticity produced by the free-slip condition (Epifanio 2007). This vorticity has very little effect on the flow and is not included in this description.
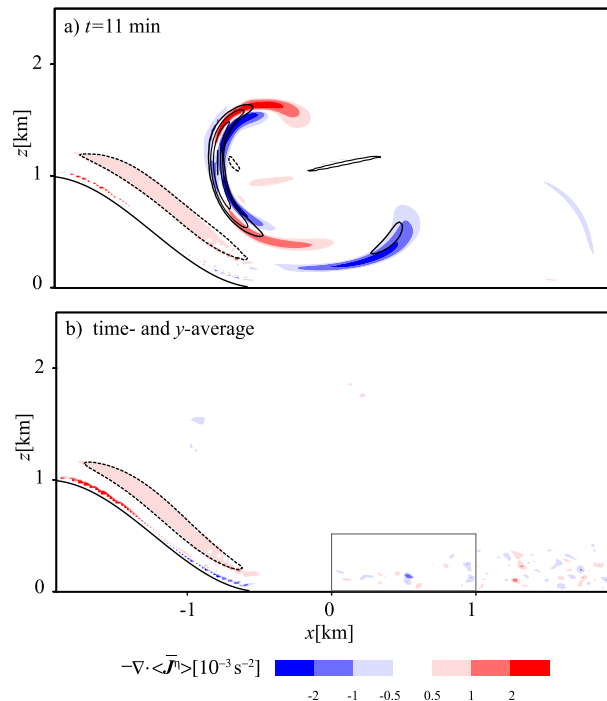

FIG. 8. Budget for $\langle\eta\rangle$ (a) at $t = 11$ min and (b) averaged over $t = 30$–60 min, with the transport terms in color shading and the baroclinic term in contour lines indicating values of $-0.5, 0.5, 1.0, 2.0, 3.0 \times 10^{-3}$ s^{-2}, with the negative value indicated by the dashed contour line. Note that before the onset of turbulence in (a), $\langle\mathbf{J}^\eta\rangle = \mathbf{J}^\eta$. The box in (b) indicates the domain over which the time- and x-averaged contributions to (12) are given in Fig. 9.

permanent change to the flow downstream (EQ08, p. 3152).

In the statistically steady state, Fig. 8b shows that the time- and y-averaged baroclinic generation and transport upstream of the hydraulic jump continue to act just as they did in the earlier evolution of the flow. However, in and downstream of the hydraulic jump, these terms are nearly zero, consistent with a statistically steady state. To obtain a better understanding of how these terms sum to zero, we consider that, assuming statistical stationarity,

$$\langle\overline{\mathbf{J}^\eta}\rangle = \big(\langle\overline{u}\rangle\langle\overline{\eta}\rangle + \langle\overline{u'\eta' - \upsilon'\xi'}\rangle - \nu\partial_x\langle\overline{\eta}\rangle, \langle\overline{w}\rangle\langle\overline{\eta}\rangle$$
$$+ \langle\overline{w'\eta' - \upsilon'\zeta'}\rangle - \nu\partial_z\langle\overline{\eta}\rangle\big), \qquad (14)$$

where $\langle\upsilon\rangle = 0$ because of statistical homogeneity in the y direction. Figure 9 shows the average from $x = 0$ to $x = 1$ km (the box in Fig. 8b) of the individual contributions to $-\nabla\cdot\langle\overline{\mathbf{J}^\eta}\rangle$, as well as the time-averaged baroclinic generation $-\partial_x\langle\overline{b}\rangle$. This figure makes it clear that the main balance in (12) in the statistically steady state is between the mean- and eddy-advection terms,
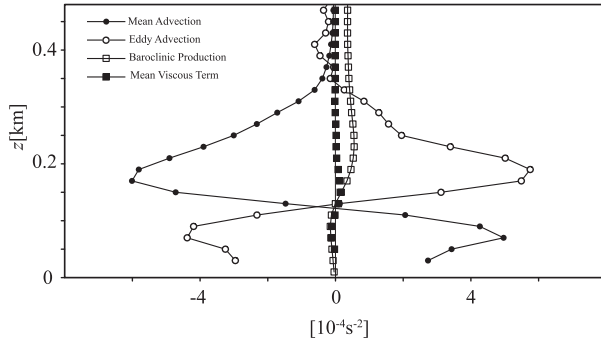
FIG. 9. Average from $x = 0$ to $x = 1$ km of the contributions to the rhs of (12) in the statistically steady state over the window indicated by the box in Fig. 8b. The baroclinic production term is indicated by the open squares; from (14), the individual contributions to $-\nabla \cdot \langle \mathbf{J}^\eta \rangle$ are the mean transport (filled circles), eddy transport (open circles), and the mean viscous term (filled squares).

with buoyancy and direct friction playing relatively minor roles.

In the classical theory of the hydraulic jump (Rayleigh 1914), a single layer is envisioned to undergo a discontinuous adjustment from supercritical ($u/\sqrt{gh} > 1$) to subcritical ($u/\sqrt{gh} < 1$) flow. Mass and momentum are conserved through the discontinuity, but energy is dissipated. From the time- and y-averaged NSE [(6)–(8)], the following energy equation can be formed:

$$\langle \overline{\mathbf{u}} \rangle \cdot \nabla B = -\frac{g}{\theta_{00}} \langle \overline{z}_\psi \rangle Q_t + \langle \overline{\mathbf{u}} \rangle \cdot \mathbf{F}, \qquad (15)$$

where

$$B = \frac{1}{2} \langle \overline{\mathbf{u}} \rangle \cdot \langle \overline{\mathbf{u}} \rangle + \langle \overline{P} \rangle - \langle \overline{b} \rangle \langle \overline{z}_\psi \rangle, \qquad (16)$$

$$Q_t = -\partial_x \langle \overline{u'\theta'} \rangle - \partial_z \langle \overline{w'\theta'} \rangle, \qquad (17)$$

$$\mathbf{F} = \left(-\partial_x \langle \overline{u'u'} \rangle - \partial_z \langle \overline{u'w'} \rangle, -\partial_x \langle \overline{u'w'} \rangle \right.$$
$$\left. - \partial_z \langle \overline{w'w'} \rangle \right), \qquad (18)$$

where z_ψ is the height of the streamline; direct viscous effects on the mean variables are negligible and thus not included in (17) and (18).[4] The quantity B is the Bernoulli function composed of time- and y-averaged variables; (15) indicates the variation of B along time- and y-averaged streamlines will occur as a consequence of turbulent heat and/or momentum transfer. Figure 10a shows that the sum of the terms on the rhs of (15) act to decrease B along the flow and that the effect is

----

[4] It may be shown that $\mathbf{F} = \left(-\langle \overline{w'\eta' - v'\zeta'} \rangle, \langle \overline{u'\eta' - v'\xi'} \rangle \right)$ so that the turbulent diffusion of $\langle \eta' \rangle$ in Fig. 9 can be interpreted in terms of the derivatives of the eddy momentum fluxes.
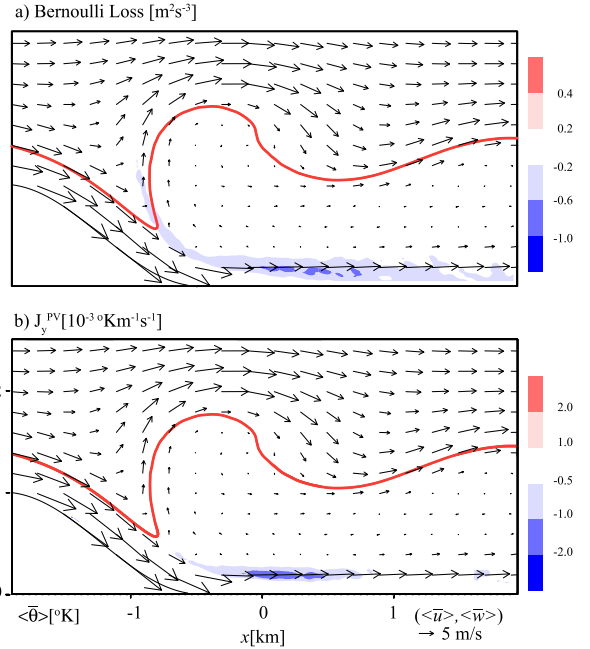

a) Bernoulli Loss [m²s⁻³]

b) J_y^{PV} [10⁻³ °Km⁻¹s⁻¹]

FIG. 10. Analysis of the time- and y-averaged (a) Bernoulli loss [rhs of (15)] and (b) spanwise flux of potential vorticity J_y^{PV} in (10).

concentrated on the lower branch of the flow where the tke is the strongest (Fig. 7b). To compute the heating term (not shown), we estimate the displacement of the streamlines that reach to the turbulent zone is $\langle \overline{z}_\psi \rangle \approx -1000$ m; the heating term has both positive and negative contributions but is generally smaller in magnitude than the frictional term in (15). Dissipation in the lower layer in association with a upstream-directed wave overturning is consistent with the two-dimensional parameterized diffusion experiments of Klemp et al. (1997, their Fig. 16). These results are also qualitatively very similar to those shown in Figs. 11d and 11e of EQ08 in the analysis of Bernoulli function decreases in the case of a breaking mountain wave.

A related diagnostic quantity discussed in the literature (EQ08) is the turbulent cross-stream flux of potential vorticity ($\omega \cdot \nabla \theta$):

$$J_y^{PV} = \partial_z \langle \overline{\theta} \rangle F_x - \partial_x \langle \overline{\theta} \rangle F_z - \langle \overline{\eta} \rangle Q_t. \qquad (19)$$

Figure 7b shows that $J_y^{PV} < 0$ and is also maximized along the lower branch of the split flow, again in manner that is qualitatively similar to that found in EQ08 (their Fig. 13a).

4. Summary and conclusions

Figure 11 summarizes the evolution of the flow leading to the statistically steady leeside hydraulic jump.
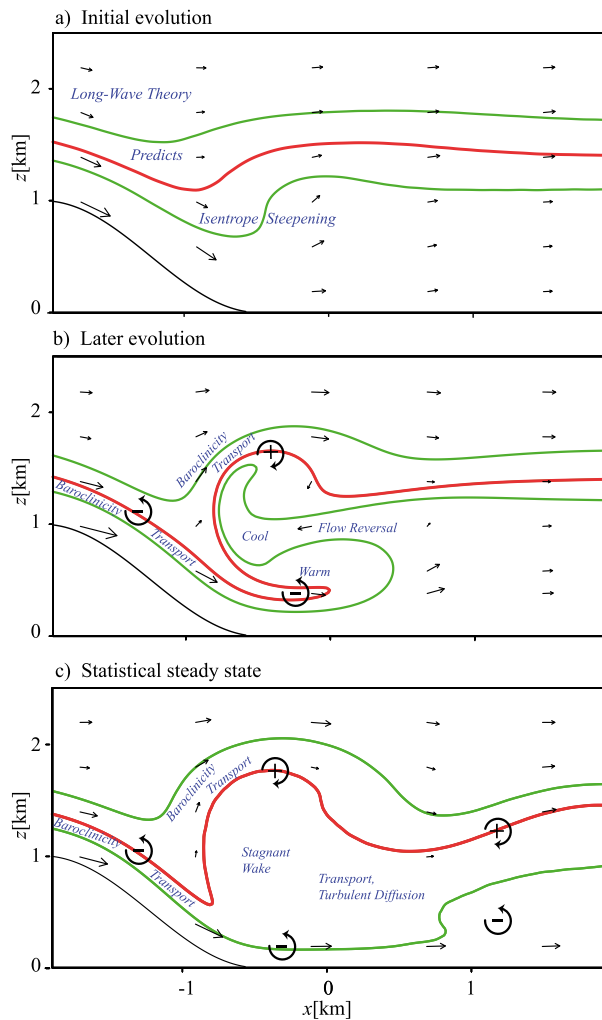
FIG. 11. (a) Schematic summary of the simulated flow associated with the hydraulic jump for the initial evolution in which long-wave theory predicts isentrope steepening. (b) As in (a), but for the early (preturbulent) evolution in which baroclinicity produces negative vorticity on the lee slope, followed by downward and leeward transport. The implied formation of reversed flow sets up baroclinicity of the opposite sign above, and thus, a vortex dipole is formed. (c) As in (a), but for the statistical steady state in which vorticity on the upstream side of the hydraulic jump remains steady. On the downstream side, the vorticity distribution is governed by mean transport and turbulent diffusion. In all panels, green and red isolines are, respectively, the bounding and central isentropes of the transition layer.

Consistent with the time-dependent SWE solutions, the time-dependent NSE solutions for the nearly identical physical problem exhibit the same tendency for leeside isentrope steepening (Fig. 11a). In contrast with the SWE, the NSE can be integrated beyond this point to reveal the internal dynamics of the leeside hydraulic jump. Figure 11b illustrates that this internal dynamics can be described by the baroclinic production of

spanwise vorticity $\eta < 0$ along the descending leeside θ surfaces; the advective transport of $\eta < 0$ toward the steepening isentropes induces reversed flow, which leads to isentropic overturning and a division of the initial transition layer into two branches characterized by a split flow–vorticity dipole with negative $\langle \eta \rangle$ below and positive above. The overturning isentropes give rise to static instability ($\partial_z \theta < 0$), and the flow downstream of this vorticity dipole eventually breaks into turbulence motions. Figure 11c illustrates that in the statistically steady state, the zone downstream of the split flow–vortex dipole is characterized by a balance between mean advection and turbulent diffusion of spanwise vorticity. Comparing Figs. 11b and 11c shows that the split flow–vortex dipole has its origin in the initially inviscid, adiabatic flow evolution and is maintained by essentially the same baroclinic production/advection mechanisms throughout the integration.

A few features of the foregoing description deserve extra emphasis. First, negative baroclinic production of vorticity along the descending leeside isentropes is the basic driving mechanism for the lower shear layer; this layer is unstable and has maximum turbulent kinetic energy (Fig. 7b). The negative vorticity in this lower layer induces via (10) the reversed/stagnant flow that splits the layer, leading to the upward-tilted isentropes at the leading edge of the jump (Fig. 7a). Hence, the upper branch is *a reaction to* the main driving influence of the lower-branch dynamics. The limited distance over which positive vorticity is created baroclinically in the upper branch (Fig. 7a) implies weaker positive vorticity, upper-branch shear, and turbulence, as compared to the lower branch. Second, the classical model of a hydraulic jump (Rayleigh 1914), based on the shallow-water equations, has a layer of uniform flow downstream, while the present simulations and laboratory studies [cited in Rotunno and Smolarkiewicz (1995)] indicate a flow minimum near the top of the lower layer. Third, the statistically stationary flow shown in Fig. 7a bears no resemblance to downstream rotors, which have in the past been associated with hydraulic jumps [see the recent review in Strauss et al. (2016)] since there is accelerated wind at the lower surface rather than a stagnation point. Rather, the internal dynamics of the hydraulic jumps simulated herein appears most similar to that of a breaking mountain wave (cf. Fig. 7a with Fig. 7 of EQ08) with respect to both the mean flow and, as mentioned several times, the analysis of the associated turbulence.

In summary, the viewpoint promoted herein is that the fundamental mechanisms for the formation of the leeside hydraulic jump are encoded in the inviscid, adiabatic equations of motion (shallow water or Navier–Stokes)

despite the common association between hydraulic jumps and energy dissipation at steady state. The present shallow-water equation simulations of the formation of the leeside hydraulic jump highlight its origins as the formation of a discontinuity that can be understood through long-wave dynamics. Integrations of essentially the same physical problem using the Navier–Stokes equations reveals the internal dynamics of the long-wave-theory-predicted discontinuity as the evolution into a split-flow–vortex dipole; instability within this structure leads to turbulence and energy dissipation. The importance of understanding the chain of causality is especially important in characterizing the causes of lee-vortex formation in two-layer flow. The latter is the subject of Part II.

REFERENCES

Baines, P. G., 1995: *Topographic Effects in Stratified Flow.* Cambridge University Press, 482 pp.

Bryan, G. H., and J. M. Fritsch, 2002: A benchmark simulation for moist nonhydrostatic numerical models. *Mon. Wea. Rev.*, **130**, 2917–2928, https://doi.org/10.1175/1520-0493(2002)130<2917:ABSFMN>2.0.CO;2.

——, and R. Rotunno, 2014: The optimal state for gravity currents in shear. *J. Atmos. Sci.*, **71**, 448–468, https://doi.org/10.1175/JAS-D-13-0156.1.

Epifanio, C. C., 2007: A method for imposing surface stress and heat flux conditions in finite-difference models with steep terrain. *Mon. Wea. Rev.*, **135**, 906–917, https://doi.org/10.1175/MWR3297.1.

——, and T. Qian, 2008: Wave–turbulence interactions in a breaking mountain wave. *J. Atmos. Sci.*, **65**, 3139–3158, https://doi.org/10.1175/2008JAS2517.1.

Houghton, D. D., and A. Kasahara, 1968: Nonlinear shallow fluid flow over an isolated ridge. *Commun. Pure Appl. Math.*, **21**, 1–23, https://doi.org/10.1002/cpa.3160210103.

Klemp, J. B., R. Rotunno, and W. C. Skamarock, 1997: On the propagation of internal bores. *J. Fluid Mech.*, **331**, 81–106, https://doi.org/10.1017/S0022112096003710.

Long, R. R., 1954: Some aspects of the flow of stratified fluids. II. Experiments with a two-fluid system. *Tellus*, **6**, 97–115, https://doi.org/10.1111/j.2153-3490.1954.tb01100.x.

Rayleigh, L., 1914: On the theory of long waves and bores. *Proc. Roy. Soc. London*, **90A**, 324–328, https://doi.org/10.1098/rspa.1914.0055.

Rotunno, R., and P. K. Smolarkiewicz, 1995: Vorticity generation in the shallow-water equations as applied to hydraulic jumps. *J. Atmos. Sci.*, **52**, 320–330, https://doi.org/10.1175/1520-0469(1995)052<0320:VGITSW>2.0.CO;2.

——, V. Grubišić, and P. K. Smolarkiewicz, 1999: Vorticity and potential vorticity in mountain wakes. *J. Atmos. Sci.*, **56**, 2796–2810, https://doi.org/10.1175/1520-0469(1999)056<2796:VAPVIM>2.0.CO;2.

Schär, C., and R. B. Smith, 1993: Shallow-water flow past topography. Part I: Vorticity production and wake formation. *J. Atmos. Sci.*, **50**, 1373–1400, https://doi.org/10.1175/1520-0469(1993)050<1373:SWFPIT>2.0.CO;2.

Stoker, J. J., 1957: *Water Waves.* Interscience, 567 pp.

Strauss, L., S. Serafin, and V. Grubišić, 2016: Atmospheric rotors and severe turbulence in a long deep valley. *J. Atmos. Sci.*, **73**, 1481–1506, https://doi.org/10.1175/JAS-D-15-0192.1.

Townsend, A. A., 1976: *The Structure of Turbulent Shear Flow.* Cambridge University Press, 429 pp.

Tschantz, B. A., and K. R. Wright, 2011: Hidden dangers and public safety at low-head dams. *J. Dam Saf.*, **9**, 8–17.

Whitham, G. B., 1974: *Linear and Nonlinear Waves.* John Wiley and Sons, 636 pp.

Wood, I. R., and J. E. Simpson, 1984: Jumps in layered miscible fluids. *J. Fluid Mech.*, **140**, 329–342, https://doi.org/10.1017/S0022112084000628.